Electronic Supplementary Material (ESI) for Journal of Materials Chemistry C.
This journal is © The Royal Society of Chemistry 2021

Supporting Information

High-throughput calculations of spintronic tetra-phase transition metal dinitrides

Junfei Ding,[1] Qiushi Yao[2], Huasheng Sun [1], Shanbao Chen[1], Fang Wu[3], Chengxi Huang*[1] , Erjun Kan*[1]

[1] MIIT Key Laboratory of Semiconductor Microstructure and Quantum Sensing and Department of Applied Physics, Nanjing University of Science and Technology, Nanjing 210094, P. R. China

[2] Department of Physics, Southern University of Science and Technology, Shenzhen 518055, Guangdong, P. R. China

[3] College of Information Science and Technology, Nanjing Forestry University, Nanjing, Jiangsu 210037, P. R. China

Correspondence and requests for materials should be addressed to

E. K. (ekan@njust.edu.cn), C. H. (chuang@njust.edu.cn)

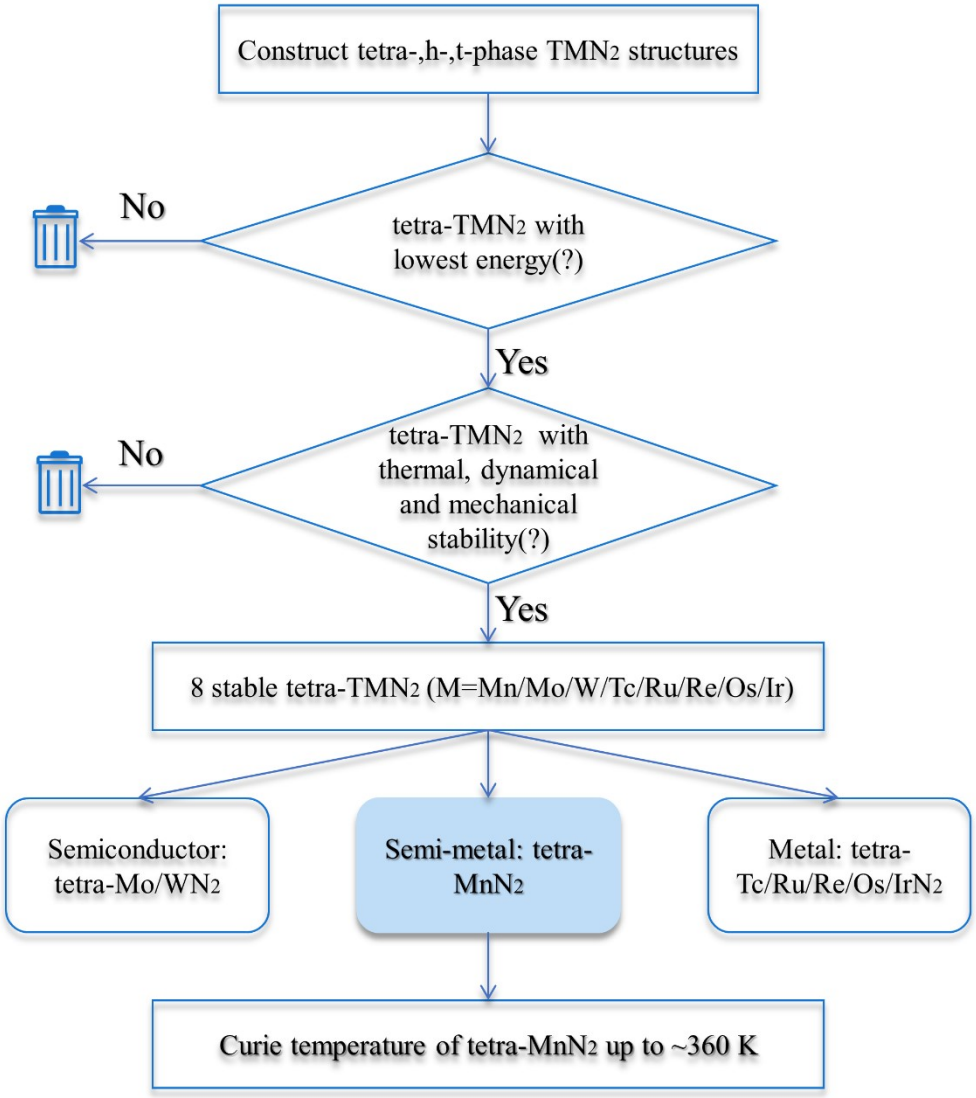

Figure S1. The workflow used to calculate the structure and properties of tetra-TMN_2. The trash symbol indicates the material is not included in the following process at all.

In **Figure S1** we displayed the workflow of the calculation process of tetra-TMN_2. First of all, we construct the initial structures of h-,t- and tetra-phase TMN_2 by our costom code. And then, we optimized the cell lattice constants and atom positions of the structures. As shown in workflow, for the first round selection, the tetra-phase structures with lower energy compared to that of h- and t-phase are selected. For the second selection, only the tetra-phase structures with thermal, dynamical and mechanical stability are chosen. Ffter these two slection, we get 8 tetra-phase stuctures, and then their correspongding properties are calculated.

3d		Sc	Ti	V	Cr	**Mn**	Fe	Co	Ni	Cu	Zn
	H	-21.975	-22.833	-22.443	-22.387	-19.986	-17.63	-19.330	-18.088	-16.506	-21.242
	T	-18.888	-21.097	-21.711	-20.537	-20.563	-18.490	-19.344	-18.353	-17.981	-14.237
	Tetra	-17.850	-19.924	-21.242	-21.414	**-20.635**	-18.076	-17.406	-15.113	-17.384	-16.274
4d		Y	Zr	Nb	**Mo**	**Tc**	**Ru**	Rh	Pd	Ag	Cd
	H	-21.712	-25.583	-24.748	-23.683	-22.752	-20.424	-4.485	-19.829	-14.379	-8.698
	T	-19.800	-23.583	-25.356	-24.245	-22.697	-20.269	-5.774	-15.049	-11.068	-15.132
	Tetra	-18.923	-22.533	-24.698	**-24.381**	**-23.227**	**-20.8**	-5.414	-14.486	-10.492	-9.275
5d			Hf	Ta	**W**	**Re**	**Os**	**Ir**	Pt	Au	Hg
	H		-27.113	-27.289	-27.311	-26.151	-23.982	-20.374	-16.158	-18.611	-16.356
	T		-25.800	-27.986	-28.056	-25.932	-23.583	-20.600	-17.380	-12.919	-8.732
	Tetra		-24.601	-27.170	**-28.257**	**-26.423**	**-24.186**	**-20.943**	-16.878	-11.729	-7.734

Table S1. Total energy(eV) of the h-TMN_2, t-TMN_2 and tetra-TMN_2 of each element in 3d, 4d and 5d period table.

The elements in this table are arranged as their original position in period table. The elements which have lower energy of tetra-phase and the energy of tetra-TMN_2 are in green bold letters.

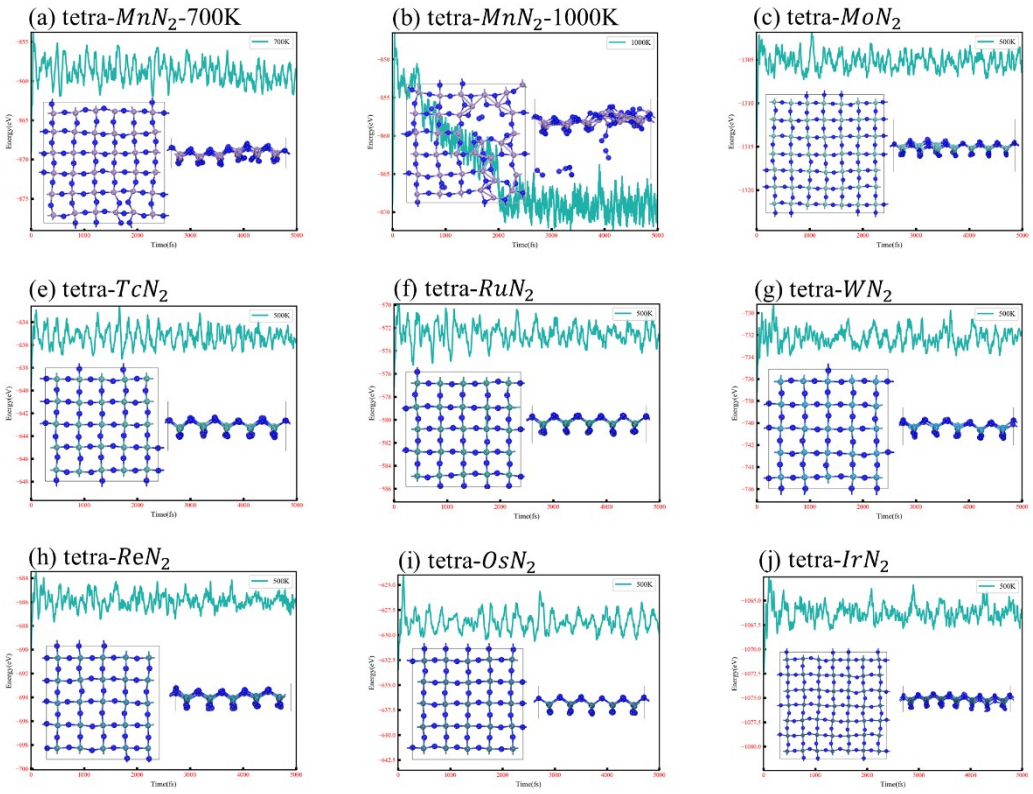

Figure S2. Variation of the total potential energy of tetra-TMN_2 in terms with simulation time during AIMD simulation. (a) and (b) for tetra-MnN_2 at 700 K, 1000 K, respectively. (c)-(j) for tetra-M(M=Mo, Tc, Ru, W, Re, Os and Ir)N_2 at 500 K, respectively. The insets are the top and side views

of the geometrical structures at the end of simulation.

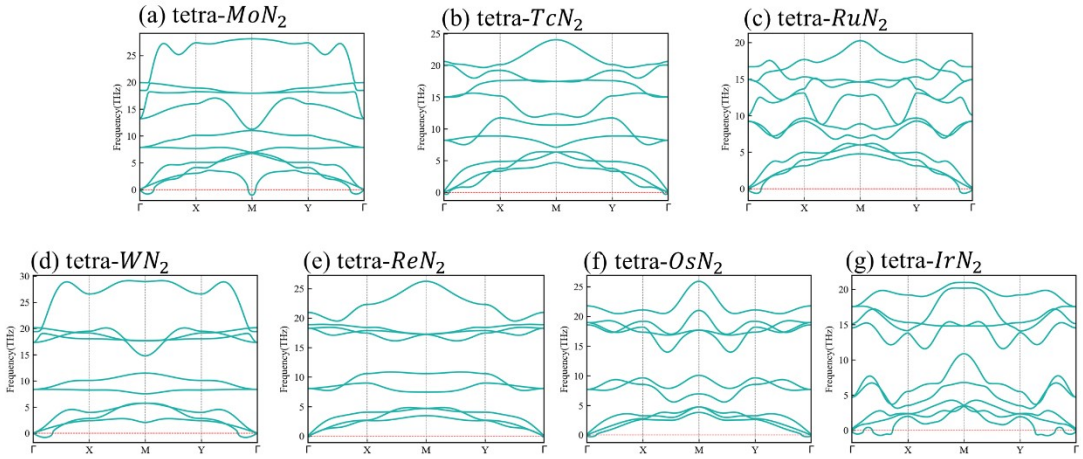

Figure S3. Phonon band structures of tetra-MN_2 monolayer.

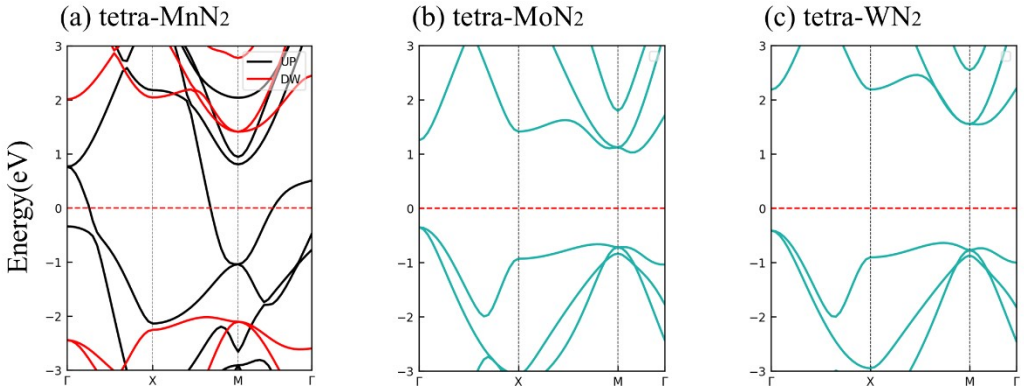

Figure S4. Band structures of (a) tetra-MnN_2, (b) tetra-MoN_2 and (c) tetra-WN_2 calculated by HSE06.

	C_{11}	C_{22}	C_{12}	C_{66}	E	ν
tetra-MnN_2	117.0	117.0	17.4	26.1	114.4	0.15
tetra-MoN_2	88.4	88.4	7.5	18.4	87.7	0.08
tetra-TcN_2	130.1	130.1	10.9	19.0	129.2	0.08
tetra-RuN_2	101.4	101.4	37.5	13.9	87.5	0.37
tetra-WN_2	102.6	102.6	9.5	19.5	101.7	0.09
tetra-ReN_2	108.8	108.8	23.7	21.1	103.6	0.22
tetra-OsN_2	90.4	90.4	28.7	12.9	81.3	0.32
tetra-IrN_2	77.5	77.5	19.8	10.2	72.4	0.26
Graphene	352.7	352.7	63.0	144.8	341.4	0.18

Table S2 Elastic constants C (Nm^{-1}), in-plane Young's modulus E (Nm^{-1}) and Poisson's ratio ν of tetra-MN_2.

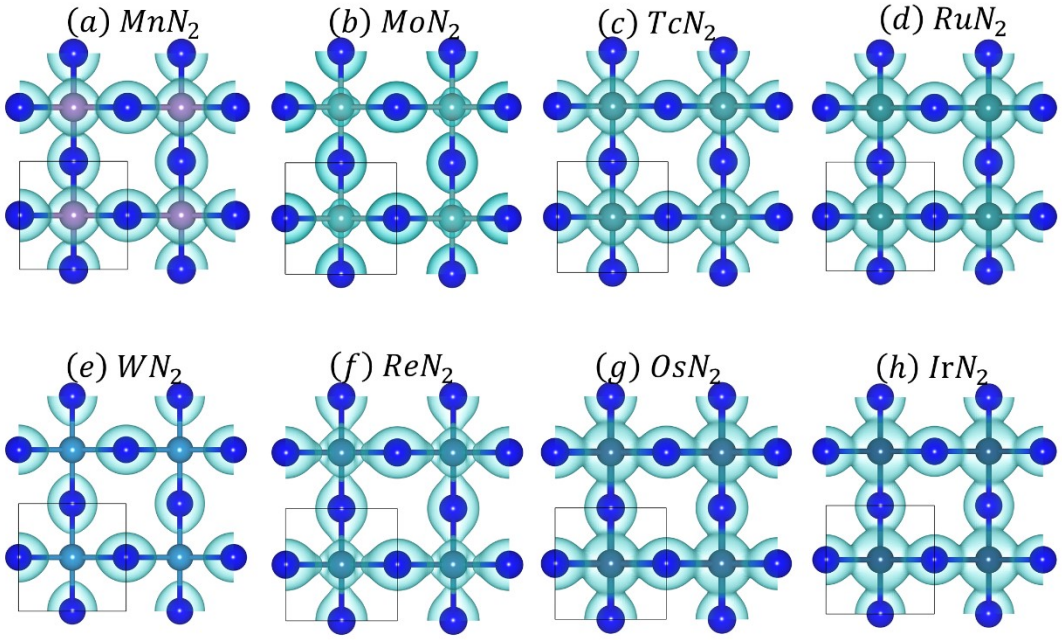

Figure S5. Spatial distribution of electron density with an isosurface of 0.12 e/$Å^3$ of tetra-MN_2

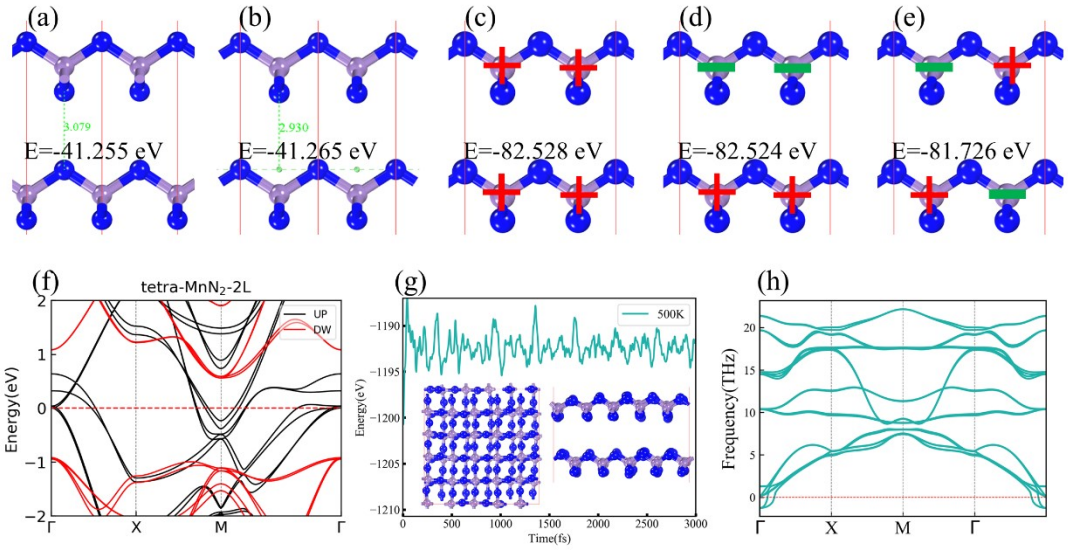

Figure S6. (a) and (b) are side view of the bi-tetra-MnN_2 with AB-stacked and AA-stacked configuration, respectively, the total energy and interlayer spacing of these two structures are also marked in the pictures. (c), (d) and (e) are the three magnetic configurations of bi-tetra-MnN_2 respectively, red crosses denote the spin-up sites and green short lines denote the spin-down sites, the total energy E of the corresponding structures are also marked in pictures. (f) Band structures of bi-tetra-MnN2. (g) Variations in total energy versus time for AA-stacked bi-tetra-MnN_2 in ab initio molecular dynamics (AIMD) simulations at 500 K; insets represent the top and side views of

snapshots at the end of AIMD simulations of 3 ps. (h) Phonon dispersion of the AA-stacked bi-tetra-MnN_2.

In Figure S6 (a) and (b) we displayed the optimized tetra-MnN_2 bilayer(bi-tetra-MnN_2) with AB-stacked and AA-stacked configurations. We also marked their total energy and interlayer spacing in the figures. The AA-stacked configuration has lower total energy and shorter interlayer spacing than of the AB-stacked configuration, which means the AA-stacked configuration is more feasible. From the molecular dynamical simulations and phonon calculation results as shown in Figure S6 (g) and (h), the AA-stacked bi-tetra-MnN_2 is thermally and thermally stable. To determine the magnetic ground state, we have considered three magnetic configurations, as shown in Figure S6 (c), (d) and (e). The results show that the ferromagnetic state in Figure S6(c) has the lowest energy, which indicates a ferromagnetic interlayer magnetic coupling. From the electronic band structure shown in Figure S6(f), the half-metallicity is also preserved in the AA-stacked bi-tetra-MnN_2.